Environ. Sci. Technol. **2003**, *37,* 2200−2208

Linking Cesium and Strontium Uptake to Kaolinite Weathering in Simulated Tank Waste Leachate

JON CHOROVER,*,† SUNKYUNG CHOI,† MARY KAY AMISTADI,† K. G. KARTHIKEYAN,‡ GARRY CROSSON,§ AND KARL T. MUELLER§

Department of Soil, Water and Environmental Science, University of Arizona, Tucson, Arizona 85721, Department of Biological Systems Engineering, University of Wisconsin, Madison, Wisconsin 53706, and Department of Chemistry, Pennsylvania State University, University Park, Pennsylvania 16802

Weathering behavior of kaolinite was studied in batch systems under geochemical conditions characteristic of tank waste released to the vadose zone at the Hanford Site, WA (0.05 M Al_T, 2 M Na^+, 1 M NO_3^-, pH ∼14, Cs^+ and Sr^{2+} present as co-contaminants). Time series experiments were conducted from 0 to 369 d, with initial Cs^+ and Sr^{2+} concentrations ranging from 10^{-5} to 10^{-3} M. Dissolution of kaolinite increased soluble Si and Al to maximum levels at 7 d (Cs and Sr concentrations of 10^{-5} and 10^{-4} M) or 33 d (Cs and Sr concentrations of 10^{-3} M). Subsequent precipitation of Si and Al was coupled to the formation of oxalate-extractable solids that incorporated Cs and Sr. Strontium sorption was nearly complete within 24 h for initial Sr concentrations (Sr_0) ≤ 10^{-4} whereas Cs uptake increased over the full year of the experiment for all initial Cs concentrations. Spectroscopic analyses revealed neoformed solids including the zeolite Na−Al silicate (Al-chabazite), and feldspathoids sodium aluminum nitrate silicate (NO_3-sodalite), and sodium aluminum nitrate silicate hydrate (NO_3-cancrinite), which can incorporate Cs. Single-pulse ^{27}Al solid-state nuclear magnetic resonance (NMR) spectroscopy yielded first-order rate constants (k) for mineral transformation that decreased from 3.5×10^{-3} to 2×10^{-3} d^{-1} as Cs and Sr concentrations were increased from 10^{-5} to 10^{-3} M. Discrete strontium silicate solids were also observed. The incongruent dissolution of kaolinite promoted the sequestration of contaminants into increasingly recalcitrant solid phases over the 1-yr time period.

Introduction

Clay minerals are important environmental sorbents for inorganic contaminants in soils (*1*−*4*). The presence of aluminosilicate clay minerals, such as kaolinite and smectite, in near-field soils surrounding leaking nuclear waste tanks is thought to retard the transport of radionuclides such as ^{137}Cs and ^{90}Sr (*4*−*7*). However, tank waste leachate at many important U.S. Department of Energy sites (e.g., Hanford, WA; Savannah River, GA; Oak Ridge, TN) is composed of solutions that are unique in having extremely high pH and ionic strength (*7*). Contaminant sorption (defined here as uptake to the solid phase) under these conditions is likely to be affected by mineral transformation reactions that are not well-known.

The effect of alkaline solutions on kaolinite transformation has been investigated previously (*8*−*12*). For example, Bauer et al. (*12*), examined kaolinite weathering over several months at 35 and 80 °C in 0.1−4 M KOH solutions and at solid−solution ratios ranging from 1:80 to 1:240. They reported the formation of illite, followed by KI-zeolite and phillipsite and then precipitation of the stable product K-feldspar. The aqueous chemistry of caustic tank waste leachate is dominated by Na^+, $Al(OH)_4^-$, and NO_3^- with variable quantities of the radionuclides ^{137}Cs and ^{90}Sr. The effects of these constituents on kaolinite transformation are unknown. Furthermore, most other studies of kaolinite dissolution have focused on initial dissolution rates at pH < 12 and conditions far from equilibrium with respect to solid-phase products (*13*−*20*). As a result, there is a lack of information on dissolution and precipitation reactions in aqueous systems representative of leaking tank waste that interacts with contaminated sediments at several U.S. DOE sites.

In this study, macroscopic and spectroscopic approaches were integrated to investigate kaolinite weathering and contaminant uptake under conditions representative of waste leachate at the Hanford Site, WA.

Materials and Methods

Preparation of Kaolinite Stock Suspension. Kaolinite clay (KGa-2) from Washington County, GA, was obtained from the Source Clays Repository of the Clay Minerals Society. Prior to batch experiments, the <2-μm fraction was collected by centrifugation and cleaned to remove oxide impurities as follows. A total of 200 g of untreated clay was added to a 2-L beaker. One kilogram of ultrapure (Milli-Q) water was added, and pH was adjusted to 9.5 through the addition of small aliquots of 0.01 mol kg^{-1} NaOH to disperse the clay for size fractionation. The suspension was mixed by a magnetic stirrer for 45 min. The suspension was then transferred into 250-mL centrifuge bottles and size fractionated by centrifugation (5 min at 119*g*) to collect the fraction having an equivalent spherical diameter of less than 2.0 μm. Resuspension (at pH 9.5) and centrifugation procedures were repeated until a clear supernatant solution was obtained. The <2-μm fraction was then washed with a 1.0 mol kg^{-1} NaCl solution (adjusted to pH 3) in 250-mL centrifuge bottles for 20 min. This step was repeated until the pH value of the supernatant solution was 3. The clays were then redispersed and washed repeatedly in 0.01 mol kg^{-1} NaCl until the pH value of the supernatant solution reached 5.5. The generic structural formula for kaolinite is $[Si_4]Al_4O_{10}(OH)_8$, and KGa-2 contains some structural Fe(III) and Ti. Specific surface area of the purified sample measured using the N_2 (gas) Brunauer−Emmett−Teller (BET) method was found to be 23.2 m^2 g^{-1}.

Kinetic Batch Experiments. The use of glassware was avoided at all stages in order to prevent Si contamination. Reagent-grade $NaNO_3$, NaOH, CsCl, $SrCl_2 \cdot 6H_2O$, and $NaAlO_2 \cdot xH_2O$ were used as obtained from VWR Scientific. A consistent, CO_2–free background solution (solution concentrations prepared and reported on a mass basis) composed of ultrapure (Milli-Q) water with 2.0 mol kg^{-1} Na^+, 1 mol kg^{-1} NO_3^-, 1 mol kg^{-1} OH^-, and 0.05 mol kg^{-1} Al_T was prepared

* Corresponding author email: chorover@cals.arizona.edu; telephone: (520)626-5635; fax: (520)621-1647.
† University of Arizona.
‡ University of Wisconsin.
§ Pennsylvania State University.

10.1021/es025980x CCC: $25.00
Published on Web 04/15/2003

to simulate the chemistry of observed tank waste leachate (*7*). This synthetic tank waste leachate (STWL) was spiked to give three initial aqueous-phase Cs^+ and Sr^{2+} concentrations, where each contaminant was added at a level of 10^{-5}, 10^{-4}, or 10^{-3} M, and both cations were present in all systems. Batch experiments were conducted in sealed 60-mL polypropylene copolymer (PPCO) bottles. Batch reactors contained 0.5 g dry mass of clay suspended in 25.0 g of STWL solution, yielding a solid to solution mass ratio of 1:50. Six replicate reactors were used, comprising duplicate sets for (i) wet chemistry analysis, (ii) solid-phase analysis after reaction, and (iii) solid-phase analysis after post-reaction acid ammonium oxalate extraction.

The bottles were placed on an end-over-end shaker at 2 rpm, and separate reactors were sampled after 1, 7, 33, 93, 190, and 369 d. At the termination of a given reaction period, clay suspensions were transferred to PPCO centrifuge tubes and centrifuged at 28700*g* for 20 min. The supernatant solution was filtered through a 0.2-μm PTFE syringe filter and acidified to pH 1.5 with trace metal grade HNO_3. In preparation for solid-phase analyses, the centrifuged pellets were first resuspended in 95% ethanol (adjusted to pH 10 with 1 M NaOH) to remove entrained salt solution. Two more ethanol washes were conducted without pH adjustment. Two samples were removed, dispersed in 15 mL of Milli-Q water, frozen immediately at −80 °C, and then freeze-dried for solid-phase analysis. The remaining samples were subjected to resuspension in 33 g of 0.1 M $Mg(NO_3)_2$, shaken for 1 h, and then centrifuged at 28700*g* for 20 min to extract readily exchangeable Cs and Sr. The supernatant solution was collected and acidified with concentrated HNO_3 to pH 2. Pellets were washed three times with 95% ethanol prior to being resuspended in 0.2 M acidic ammonium oxalate solution (AAO) (4 h at pH 3 on a reciprocal shaker in the dark) to extract poorly crystalline (or short-range ordered) precipitates (*21*). The samples were centrifuged at 28700*g* for 20 min, and the supernatant solution was acidified to pH 1. Residual solids were washed successively with 0.1 and 0.01 M NaCl solution to remove ammonium oxalate, followed by three 95% ethanol washes prior to freeze-drying for solid-phase analysis.

Solution and Solid-Phase Analysis. An Accumet solid-state electrode with a Si-free glass bulb was calibrated by Gran titration of NaOH solution at the experimental ionic strength for direct measurement of OH^- concentration. Silicon concentrations in the reacted and AAO extraction solutions were determined by inductively coupled plasma atomic emission spectrometry (ICP-AES) using a Thermo Jarrell Ash model 61E. Analysis of the reacted solid phase involved a multi-faceted approach. X-ray diffraction (XRD) analysis was conducted on randomly oriented powder samples mounted on zero background quartz slides using a Scintag diffractometer with Cu Kα radiation, a Pad X-418, θ-2-θ goniometer with a Ge solid-state detector at 35kV and 30mA. The divergent and receiving slit were 2.0 and 0.3 mm, respectively. Samples were scanned at 2° 2θ min^{-1} from 3° to 70° 2θ. Solid samples were also examined using scanning electron microscopy coupled with energy-dispersive X-ray spectroscopy (Philips XL-20 SEM/EDS at 25kV). X-ray element mapping was performed at 30kV using a Hitachi S 3500 N spectrometer under low vacuum (1 Pa). Diffuse reflectance infrared Fourier transform (DRIFT) spectra were obtained from 4000 to 400 cm^{-1} (optical resolution, 4 cm^{-1}) on freeze-dried samples using a Nicolet Magna 560 FTIR spectrometer after gently grinding 14 mg of sample and folding in the mass with 400 mg of KBr powder. Approximately 10 mg of freeze-dried solids was subjected to thermogravimetric analysis (TGA) on a Perkin-Elmer TGA 7 with an N_2 atmosphere, gas flow rate of 150 mL min^{-1}, temperature range between 30 and 1100 °C, and temperature step rate of 12 °C min^{-1}.

Solid-state ^{27}Al nuclear magnetic resonance (NMR) with magic angle spinning (MAS) analyses were performed on the reacted kaolinite samples using a Chemagnetics CMX-300 NMR spectrometer operating at a magnetic field strength of 7.0 T and a ^{27}Al resonance frequency of 78.4858 MHz. The low-frequency channel of a 4 mm Chemagnetics HX double-resonance MAS probe was used. Single-pulse ^{27}Al spectra were measured using short radio frequency pulses of 0.83 μs (equivalent to a 15° tip angle for the central transition), a spinning rate of 14.00 kHz, and a recycle delay of 1.0 s. Free induction decays of 1024 data points were processed with an exponential windowing function corresponding to a line broadening of 50 Hz. The ^{27}Al chemical shifts (in ppm) are referenced to an external sample of 1 M $Al(H_2O)_6^{3+}$. The use of short radio frequency pulses ensures accurate quantification of the resonances from four- and six-coordinate aluminum, which can have substantially different quadrupolar coupling interactions (*22*).

Results and Discussion

Silicon and Aluminum Solubility. Solution pH was relatively constant over the full range of experimental conditions and sampling periods, ranging from pH 13.5 to pH 13.7, with no clear trends over time. Soluble Si and Al concentrations increased initially with time, reached a maximum after 7 d reaction (with STWL containing 10^{-5} and 10^{-4} M Cs and Sr) or 33 d (for STWL with 10^{-3} M Cs and Sr), and then decreased (Figure 1a,c). The Si and Al removed from solution after reaction were incorporated into AAO-extractable solids. The mass of Si-bearing solids increased initially and then declined (Figure 1b), presumably because of an increase in crystallinity of the secondary Si phases (and hence reduced susceptibility to dissolution in AAO). The reaction time resulting in maximum AAO-extractable Si increased from 33 to 190 d as Cs and Sr concentration increased from 10^{-5} to 10^{-3} M (Figure 1b). This suggests that an increase in the concentration of Cs and Sr in STWL slows the formation of dissolution-resistant, crystalline solids by inhibition of either kaolinite dissolution or secondary-phase precipitation. The rate of accumulation of AAO-extractable Al is also decreased by increasing contaminant concentrations, but whereas AAO-extractable Si reaches a maximum and then decreases with time, the high aqueous concentration of Al in STWL promotes the persistence of near maximum values of AAO-extractable Al solids even after 1 yr (Figure 1d).

Contaminant Uptake and Release. Incongruent dissolution of kaolinite was coupled to long-term Cs and Sr uptake and retention in increasingly recalcitrant solid-phase pools. The full height of bars in Figure 2 indicates the number of moles of Cs or Sr sorbed to the solid phase per unit mass of kaolinite present initially. The term *sorption* in this context implies net transfer from aqueous solution to the solid phase, potentially including both adsorption and precipitation reactions. Horizontal lines indicate sorption values that are consistent with total contaminant removal from solution.

Sorption of Sr was rapid and substantial; near total removal from solution was accomplished within 24 h for initial Sr concentrations (Sr_0) of 10^{-5} and 10^{-4} M, and 46% removal was observed for Sr_0 of 10^{-3} M (Figure 2). Even at the highest Sr_0, 93% of the Sr was sorbed by 93-d reaction time. Kinetics of Cs sorption were slower and the extent of sorption was less than for Sr, but uptake increased continuously throughout the full 369-d reaction period. After 1 yr, solids had removed 80%, 51%, and 32% of initial Cs from solution for 10^{-5}, 10^{-4}, and 10^{-3} M Cs_0 values, respectively. Cesium uptake was fit to a first-order kinetic model of the form $Cs_t = Cs_0 \exp(-kt)$, where Cs_t is the aqueous concentration of Cs at

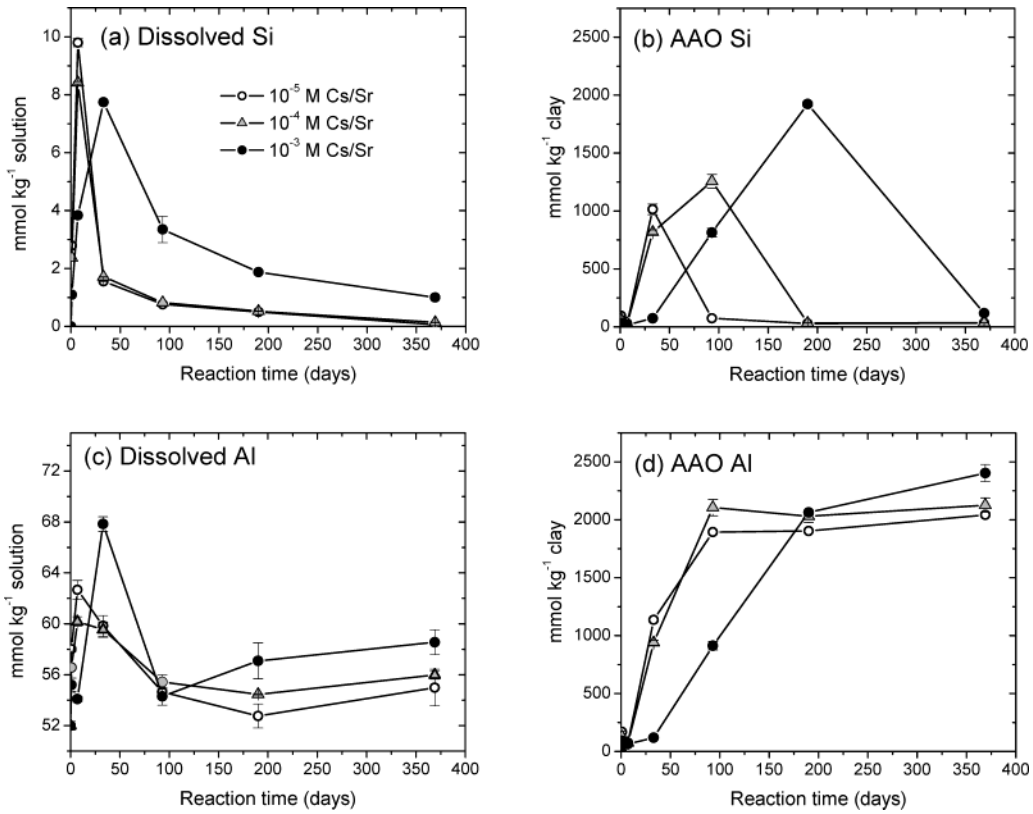

FIGURE 1. Time-dependent changes in aqueous-phase Si and Al are coupled to the formation of poorly crystalline (oxalate-extractable solids) over the 369-d reaction period: (a) dissolved Si, (b) oxalate-extractable Si in solid products, (c) dissolved Al, and (d) oxalate-extractable Al in solid products. Error bars indicate standard deviations for replicate samples.

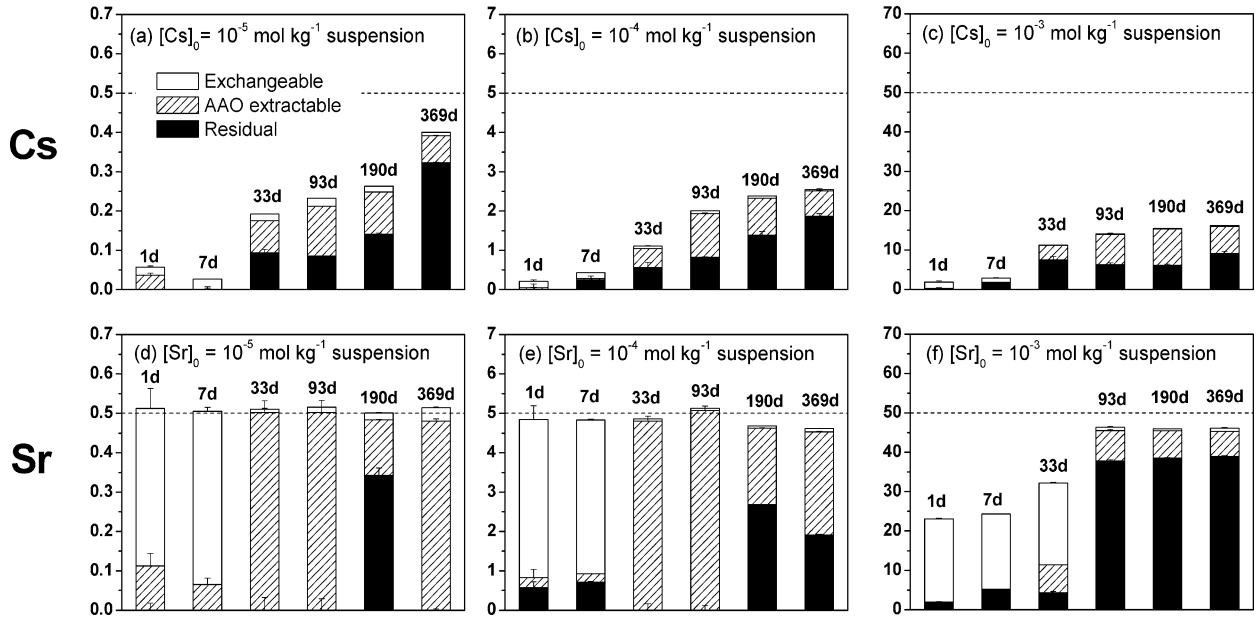

FIGURE 2. Sorption of Cs and Sr during incongruent dissolution of kaolinite in STWL. Total bar height represents millimoles of Cs or Sr sorbed to the solid phase per kilogram of kaolinite present initially (determined from concentration depletion in the aqueous phase). Complete removal from solution is represented by the horizontal lines at 0.5, 5.0, and 50.0 mmol kg^{-1} for initial contaminant concentrations of 10^{-5}, 10^{-4}, and 10^{-3} M, respectively. The millimoles of Cs and Sr recovered during Mg^{2+} exchange and AAO extraction are indicated, as is the unrecovered or "residual" mass. Error bars show standard deviations of replicate measurements.

time (t), and k is a first-order rate constant. First-order rate constants and reaction half-lives are given in Table 1.

Sequential chemical extraction of the reacted solids in $Mg(NO_3)_2$ and AAO solutions indicate that susceptibility of both Sr and Cs to desorption or dissolution decreased over the reaction period. At early times ($\leq$7 d for 10^{-5} and 10^{-4} M Sr_0 and $\leq$33 d for 10^{-3} M Sr_0), most sorbed Sr was removed by contacting the solid with unbuffered $Mg(NO_3)_2$ solution (Figure 2d–f). Later, Sr was not mobilized by ion exchange; removal required dissolution of poorly crystalline solids in AAO solution. At longer reaction time, Sr was incorporated into nonextractable pools as indicated by an increase in the

TABLE 1. First-Order Rate Constants (d^{-1}) and Half-Lives (d) for Cs Sorption and for Kaolinite Weathering in STWL[a]

Cs_0 and Sr_0 (mol kg^{-1})	first-order rate constant, k (d^{-1})		reaction half-life, $t_{1/2}$ (d)	
	Cs sorption	^{27}Al NMR	Cs sorption	^{27}Al NMR
10^{-5}	4.09×10^{-3}	3.51×10^{-3}	169	197
10^{-4}	1.93×10^{-3}	3.42×10^{-3}	359	203
10^{-3}	0.99×10^{-3}	1.97×10^{-3}	699	351

[a] Weathering rates were calculated from ratio of $^{27}[Al^{IV}/(Al^{IV} + Al^{VI})]$ MAS NMR peak intensities of reacted solids. All regressions resulted in $R^2 > 0.8$ and $p < 0.01$.

residual fraction. For Cs, an increase in the residual pool accompanied the time-dependent increase in overall sorption (Figure 2a–c). These results indicate that both contaminants are being incorporated into increasingly recalcitrant solid phases over the long term via coupling to weathering-induced mineral transformations, as also suggested by major element dissolution and precipitation data (Figure 1).

X-ray Diffraction and Infrared Analysis. Figure 3 shows XRD patterns of the solid phase for selected reaction times before and after oxalate extraction. The time series of XRD patterns for all samples is provided in Figure 1 of the Supporting Information. Reaction with STWL induced a decrease in intensity of kaolinite ($t = 0$ d) XRD peaks (*23*) and emergence of new peaks, beginning at 33 d, attributable to three feldspathoid or zeolite phases: sodium aluminum silicate (zeolite Al-chabazite; $Na_{39.8}Al_{70.4}Si_{41.2}O_{207.9}$) (*24*), sodium aluminum nitrate silicate (feldspathoid sodalite; $Na_8[AlSiO_4]_6(NO_3)_2$) (*25*), and sodium aluminum nitrate silicate hydrate (feldspathoid cancrinite; $Na_8(Al_6Si_6O_{24})(NO_3)_2 \cdot 4H_2O$) (*26*). While Al-chabazite and nitrate sodalite were the predominant solids formed at the highest Cs/Sr loading, XRD peak intensities for nitrate sodalite were consistently greater at lower Cs and Sr concentration. At the highest contaminant concentration, Al-chabazite precipitation was followed by emergence at 190 d of nitrate sodalite peaks (Figure 3 and Supporting Information Figure 1). Diminished relative intensity and broadening of the d-001 basal spacing of kaolinite were concurrent with the formation of secondary minerals.

Bickmore et al. (*27*) reported the formation of nitrate cancrinite during weathering of quartz in simulated Hanford tank solutions, but they did not explore effects of contaminant concentrations, and solid-phase incorporation of NO_3 (relative to the more common CO_3 anion) was inferred from their CO_2-free experimental conditions. In the present case, solid-phase incorporation of nitrate has been verified directly using DRIFT spectroscopy. The full time series of DRIFT spectra for reacted solids (see Supporting Information Figure 2) show absorption bands at 1383 and 1424 cm^{-1} that increase with time, which can be assigned to growth of nitrate-containing cancrinite or sodalite (*28*, *29*). Chabazite XRD peak intensities are weak and overlap with the other secondary phases but match most closely with the Al-rich chabazite. Oxalate extraction data (Figure 1) indicate a molar Si/Al ratio of <1 for this sample, and thermogravimetric analyses suggest that this phase is also hydrated. Therefore, the chabazite detected is apparently not identical to phases currently contained in the International Center for Diffraction Data (ICDD) database.

Cancrinite belongs to the hexagonal crystal system and space group $P6_3$ with AB–AB layer-type packing (*30*–*32*). Large channels and a series of cages run parallel to the *z*-axis (*31*). Sodalite, which has a cubic crystal structure (space group $P\bar{4}3n$), lacks channels due to its ABC layer packing but has a network of large cages (*33*, *34*). Charge balancing cations occupy the channels and cages. Relative peak intensities and unit cell dimensions derived from XRD depend not only on the structure of the framework but also on the extent of structural water incorporation and the amount and type of species present in the framework channels and cages (*33*). In our experimental system, sodalite and cancrinite can be formed from crystallization of soluble silica and aluminate with NO_3^-, OH^-, and H_2O. Although some CO_3^{2-} incorporation is possible, atmospheric CO_2 was largely excluded from

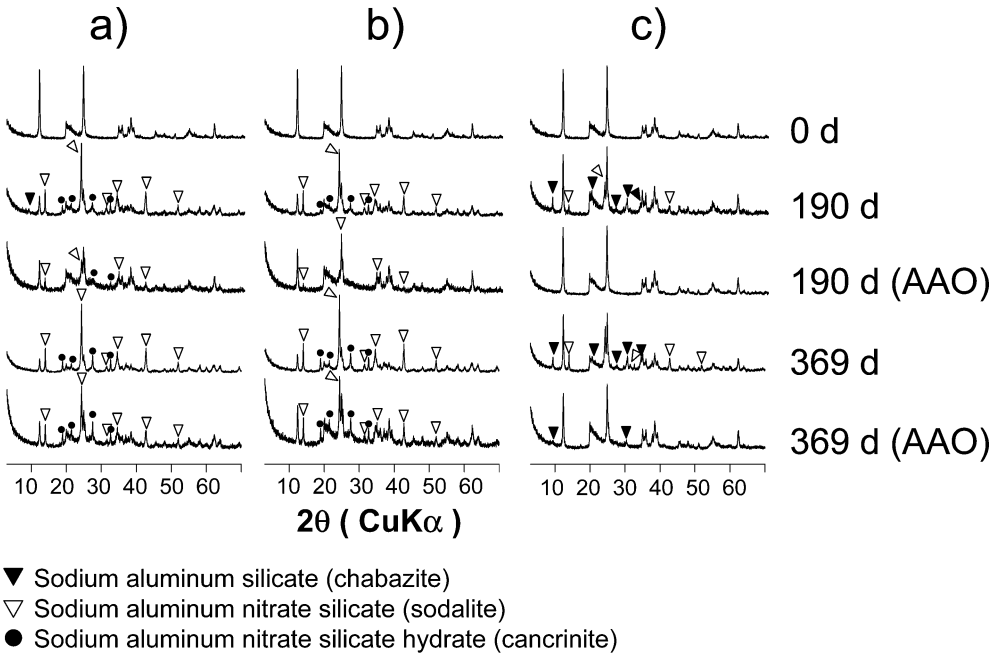

FIGURE 3. X-ray diffraction patterns of kaolinite and solid-phase products at selected reaction times ($t = 0$, 190, and 369 d). XRD patterns are also shown for the same samples after reaction with AAO (no effect was observed for the $t = 0$ sample; it is not shown). Initial Cs and Sr concentrations are (a) 10^{-5}, (b) 10^{-4}, and (c) 10^{-3} M. (▼) sodium aluminum silicate (chabazite), (▽) sodium aluminum nitrate silicate (sodalite), and (●) sodium aluminum nitrate silicate hydrate (cancrinite).

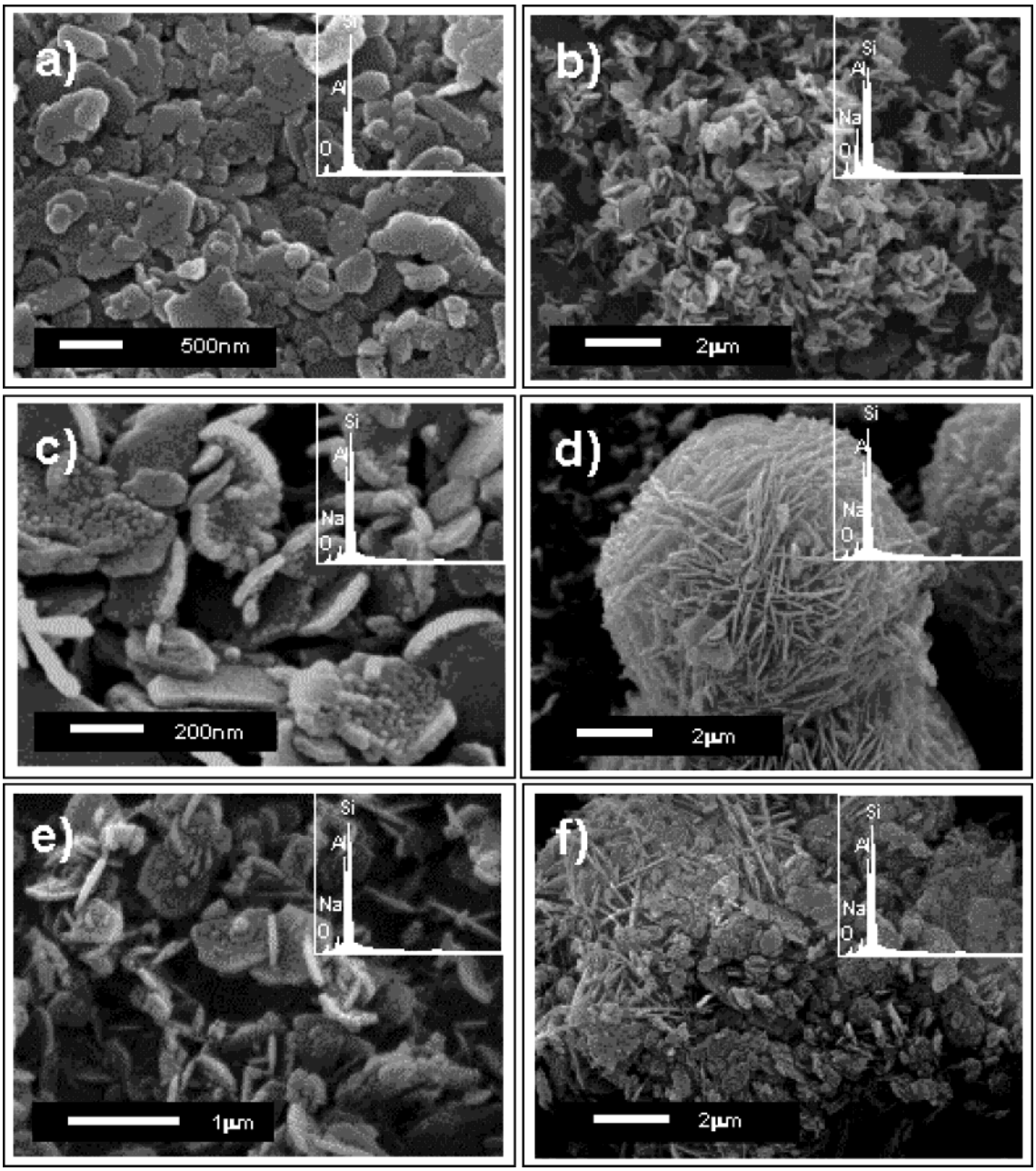

FIGURE 4. SEM images with EDS spectra of (a) poorly crystallized particles of unreacted kaolinite, (b) platy cancrinite in reacted kaolinite systems with 10^{-5} M Cs and Sr after 190 d, (c) fine sodalite crystals on kaolinite and cancrinite surfaces at 10^{-5} M Cs and Sr after 190 d, (d) Al-chabazite-containing precipitates at 10^{-3} M Cs and Sr after 190 d, (e) sodalite particle aggregates on the hexagonal sharp-edged cancrinite surfaces at 10^{-5} M Cs and Sr after 190 d, and (f) Al-chabazite with kaolinite particles at 10^{-3} M Cs and Sr after 369 d.

the reaction vessel, and aqueous-phase inorganic C concentrations were consistently less than 2 mmol L^{-1} after a full year of reaction time. Whereas Na^+ is the charge balancing cation in the chemical formulas above, substitution of Cs^+ for Na^+ is certainly possible (*35*−*37*).

The appearance of secondary phase XRD and DRIFT peaks was progressively delayed as the concentrations of Cs and Sr were increased. The time scale for diagnostic XRD peak emergence ranged from 33 d (low Cs and Sr) to 190 d (high Cs and Sr), whereas solid-phase nitrate IR bands, whose detection do not require long-range crystalline structure, were detected as early as 7 d for the low Cs and Sr case (Supporting Information Figures 1 and 2). Nitrate cancrinite peaks were not detected at 10^{-3} M Cs/Sr loading.

At early reaction times (<93 d), AAO treatment of the reacted solids resulted in complete removal of XRD peaks corresponding to neoformed precipitates. In contrast, XRD patterns for AAO extracted solids following (a) 190 and (b) 369 d reaction time show that the growing mass of secondary phases become increasingly resistant to ligand-promoted dissolution with (i) increasing reaction time and (ii) decreasing co-contaminant concentration (Figure 3). The accumulation of Cs into AAO-resistant solids over the same time frame (Figure 2) suggests that Cs uptake is coupled to crystal growth and ripening of these zeolite and feldspathoid solids. In contrast, the fraction of Sr that resists AAO extraction is greatest for the sample of highest (10^{-3} M) initial Sr concentration (Figure 2). This suggests that Sr uptake is not as tightly coupled to growth of the same solids but may rather reflect precipitation as a separate phase. Thermodynamic modeling of initial reaction conditions with The Geochemist's Workbench (*38*) (subject to time-dependent pH constraints) indicates that for $Sr_0 \geq 10^{-4}$ M the solution is supersaturated (as a result of kaolinite dissolution) with respect to $SrSiO_3$(s).

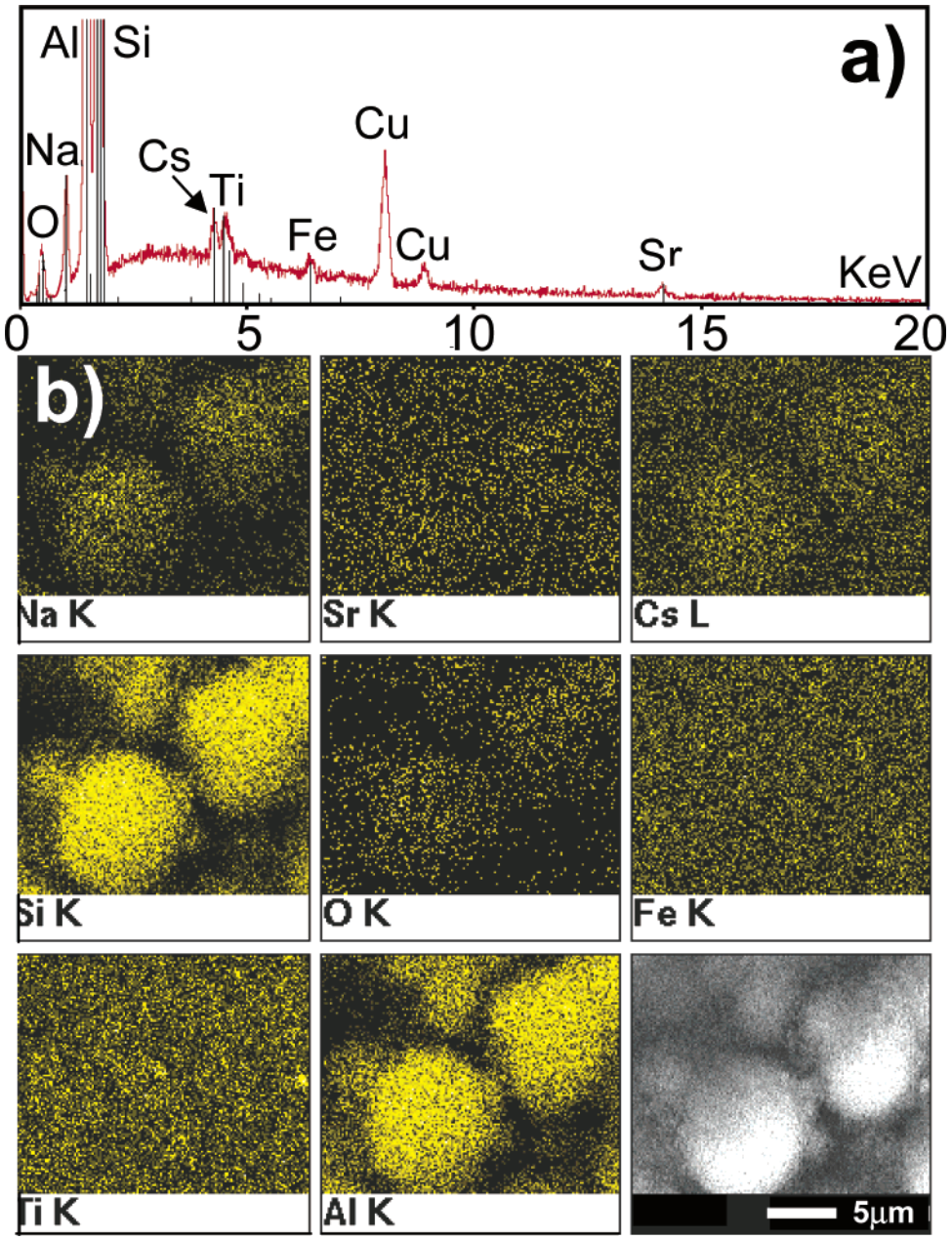

FIGURE 5. (a) EDS spectrum and mapping of Al-chabazite in reacted kaolinite systems with 10^{-3} M Cs and Sr after 190 d. (b) The elemental composition of the secondary phase is dominantly Si, Al, and Na. Accumulation of Cs is also suggested by the EDS results.

Although the rate of $SrSiO_3$(s) formation under the experimental conditions is not known, the precipitation of a hydrated precursor may be favored kinetically. Assuming that such a phase comprises (as simulations predict) 84−98% of the total Sr, then even at the highest Sr concentration, $SrSiO_3$(s) would constitute less than 1% of the solid-phase mass; therefore, it would be undetectable by XRD. Additional data that also support the formation of discrete Sr phases are discussed in the next section.

Scanning Electron Microscopy of Reacted Samples. Figure 4 shows SEM images of kaolinite unreacted (Figure 4a) and reacted at low and high Cs and Sr loadings after 190 d (Figure 4b−d). Unreacted KGa-2 comprises "poorly crystallized" kaolinite particles absent of sharp hexagonal edges. At low (10^{-5} M) Cs and Sr loading, (Figure 4b), platy nitrate cancrinite, approximately 500 nm in size, is readily observed. Newly formed nitrate cancrinite crystals are uniform in size and have sharper edges than kaolinite. At low Cs/Sr levels, nitrate sodalite exists as extremely fine crystals, averaging less than 50 nm in diameter and occurring as aggregates on kaolinite or nitrate cancrinite surfaces (Figure 4c). At the highest Cs and Sr loading, spheroidal Al-chabazite crystals of ca. 8 μm diameter are detected (Figure 4d). Fine nitrate sodalite colloids accumulate on increasingly defined cancrinite surfaces after 369 d at low Cs and Sr loadings (Figure 4e). After 369 d, spheroidal secondary phases had gradually evolved to irregular shapes (Figure 4f) at the highest Cs and Sr loading. Al-chabazite, which has isometric symmetry, appears within newly formed spheroidal particles covered with kaolinite flakes. SEM/EDS indicates that the spheroidal precipitate is composed dominantly of Si, Al (Si/Al mass ratio near unity), and Na, but smaller amounts of Cs are also clearly observed (Figure 5) These spheroidal precipitates are not evidently enriched in Sr (Figure 5). Following AAO treatment, spheroidal secondary minerals were not observed, indicating that this solid exhibits more rapid ligand-promoted dissolution kinetics (at pH 3) than the other solid-phase products. In addition to these Cs-bearing precipitates, colloidal (<2

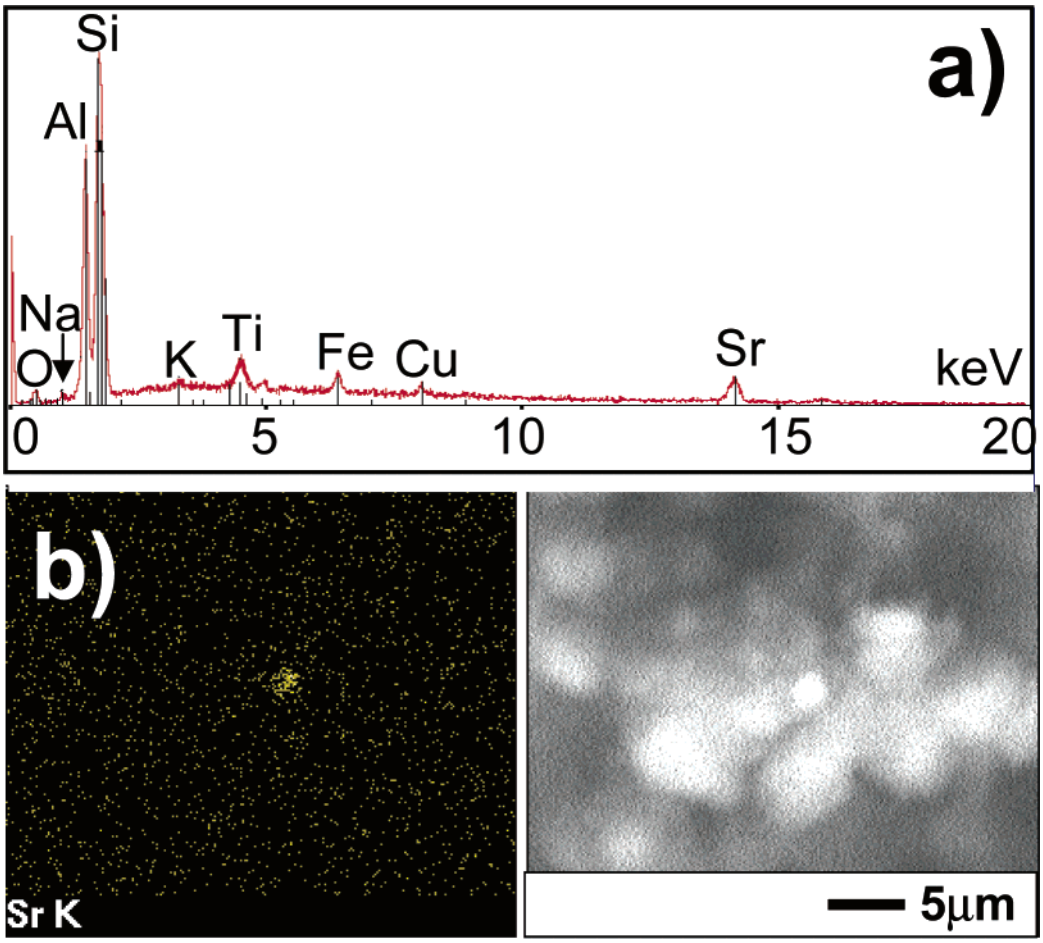

FIGURE 6. (a) EDS spectrum and mapping of particles in reacted kaolinite systems with 10^{-3} M Cs and Sr after 369 d. (b) The elemental composition of the secondary phase is mainly Si, Al, Na, and Sr.

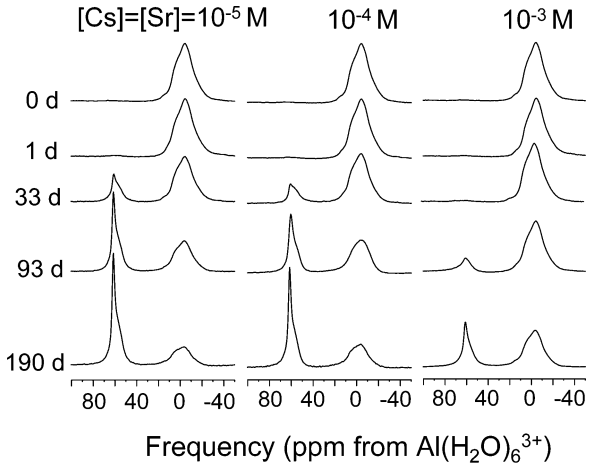

FIGURE 7. Solid-state MAS ^{27}Al NMR spectra of unreacted and reacted kaolinite (0−190 d) at Cs and Sr concentrations of 10^{-5}, 10^{-4}, and 10^{-3} M.

μm) particles highly enriched in Sr (but not carbonate) with a composition consistent with strontium silicate (as predicted by geochemical modeling) were also observed (Figure 6).

Mineral Transformation Rates. Solid-state ^{27}Al NMR spectra were collected on reacted kaolinite over the full range of Cs and Sr concentrations and reaction times (Figure 7). Unreacted kaolinite shows a broad resonance peak at −5 ppm from six-coordinate aluminum (Al^{VI}), with no detectable Al substitution in the tetrahedral sheet. The uneven growth with reaction time of an asymmetrical resonance near 50−65 ppm indicates the precipitation of four coordinate (Al^{IV}) in sodalite and cancrinite solids. Inspection of integrated peak intensity ratios (Al^{IV}/Al^{VI}) indicate that initial Cs and Sr concentrations strongly affect the rate at which Al^{IV} phases are formed, with more rapid precipitation at the lower Cs/Sr concentrations (Figure 7). We also collected ^{27}Al NMR spectra on AAO-treated samples (data not shown), and the results agree with XRD data, indicating that Al^{IV} solids (cancrinite and sodalite) remain after oxalate treatment only in those samples reacted for ≥190 d at lowest Cs and Sr loading.

The proportion of solid-phase Al in secondary phases was calculated as a function of reaction time and co-contaminant concentration by integrating peak area ratios ($Al^{IV}/[Al^{IV} + Al^{VI}]$) from ^{27}Al NMR data (Figure 8a). The kinetic data in Figure 8a are well-described by a first-order model of the form $M_{kaol,t} = M_{kaol,0} \exp(-kt)$, where $M_{kaol,0}$ and $M_{kaol,t}$ are respectively the solid-phase mass fraction of kaolinite at time zero (i.e., when $Al^{IV}/Al_T = 0$) and thereafter. Resulting calculated rate constants and half-lives for the incongruent weathering of kaolinite are given in Table 1. Overall, these results indicate that, despite the very high (2 M) background concentration of Na^+ in STWL, weathering behavior of kaolinite clay and neoformation of secondary solids exhibits a strong negative dependence on much lower concentrations (10^{-5}−10^{-3} M) of target contaminants (Cs and Sr).

We postulate that Cs and Sr play distinct geochemical roles to affect the observed coupling between contaminant sorption and mineral transformation. Strontium adsorption, which is rapid and near complete prior to detectable kaolinite weathering, appears to diminish kaolinite dissolution rate. Sorbing metal cations may inhibit mineral dissolution at

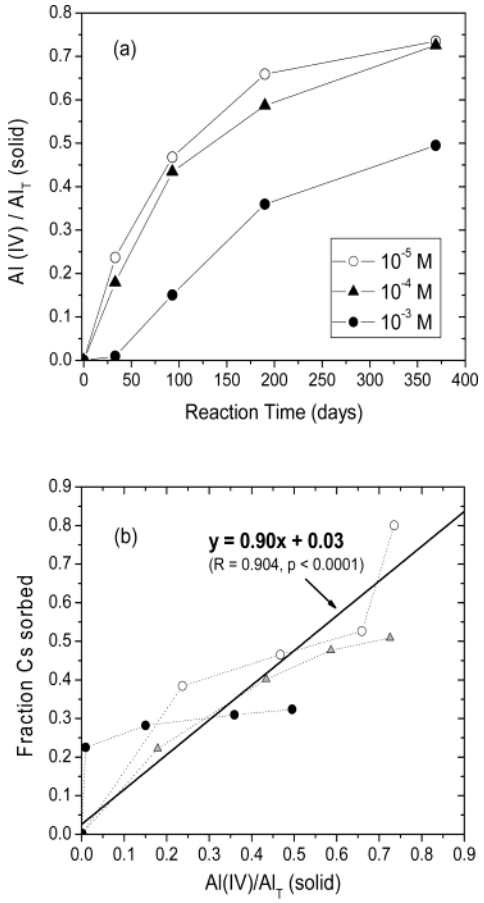

FIGURE 8. (a) Al(IV)/(Al(VI) + Al(VI)) ratio in reacted kaolinite as a function of reaction time and co-contaminant concentration as measured by NMR. The ratio increases over time, indicating the relative increase of tetrahedrally coordinated Al in the solid phase. (b) Correlation between Cs uptake to solid phase (as a mass fraction of Cs_0) and formation of tetrahedral Al solid-phase products. Initial Cs concentrations are indicated, but regression equation includes all data points irrespective of Cs_0.

acidic pH by displacing surface protons (*39*), but a mechanism for alkaline conditions has not been proposed. Tits et al. (*40*) also reported Sr retention by calcium silicate hydrate phase formations when quartz portlandite was reacted at pH 13. Coprecipitation of dissolved Si and Al incorporates Cs during secondary mineral growth and, therefore, Cs exhibits slow uptake kinetics that correlate with the formation of secondary solids as tracked by ^{27}Al NMR (Figure 8b). The rate of Cs uptake (in mol kg^{-1} d^{-1}) is proportional to its initial concentration in solution, suggesting stoichiometric exchange of Cs^+ for Na^+ during growth of zeolites and feldspathoids. Strontium appears to be precipitating as a separate strontium aluminum silicate phase that is not detectable by XRD.

Molecular-scale speciation of Cs and Sr in these solids is therefore an important objective for future studies on radionuclide fate in soil systems impacted by caustic high level radioactive waste. Whereas aqueous geochemical conditions are known to influence contaminant fate, the present study highlights the effects that contaminant ions themselves can have on major element geochemistry. Through synergistic control on mineral transformation, Sr and Cs concentrations influence the rate of their own sequestration into recalcitrant solid-phase weathering products. The long-term stability of the secondary phases, which is clearly central to their environmental impact, is the subject of ongoing research.

Acknowledgments

This work was supported by the U.S. Department of Energy, Environmental Management Sciences Program Grant DE-FG07-99ER15012.

Supporting Information Available

The full time series X-ray diffraction and Fourier transform infrared spectral data on secondary phases. This material is available free of charge via the Internet at http://pubs.acs.org.

Literature Cited

(1) Lee, S. Y.; Tank, R. W. *Appl. Clay Sci.* **1985**, *1*, 145−162.
(2) Chapman, N. A.; McKinley, I. G. *The Geologic Disposal of Nuclear Waste*; John Wiley & Sons: New York, 1987.
(3) Comans, R. N. J.; Haller, M.; Depreter, P. *Geochim. Cosmochim. Acta* **1991**, *55*, 433−440.
(4) Roh, Y.; Lee, S. R.; Choi, S. K.; Elless, M. P.; Lee, S. Y. *Soil Sediment Contam.* **2000**, *9* (5), 463−486.
(5) Ames, L. L.; McGarrah, J. E.; Walker, B. A.; Salter, P. F. *Chem. Geol.* **1982**, *35*, 205−225.
(6) Cornell, R. M. *J. Radioanal. Nucl. Chem.* **1993**, *171*, 483−500.
(7) McKinley, J. P.; Zeissler, C. J.; Zachara, J. M.; Serne, R. J.; Lindstrom, R. M.; Schaef, H. T.; Orr, R. D. *Environ. Sci. Technol.* **2001**, *35*, 3433−3441.
(8) Huang, W. L. *Clays Clay Miner.* **1993**, *41*, 645−654.
(9) Carroll-Webb, S. A.; Walther, J. V. *Geochim. Cosmochim. Acta* **1988**, *52*, 2609−2623.
(10) Devidal, J. L.; Dandurand, J. L.; Gout, R. *Geochim. Cosmochim. Acta* **1996**, *60*, 553−564.
(11) Bauer, A.; Berger, G. *Appl. Geochem.* **1998**, *13* (7), 905−916.
(12) Bauer, A.; Velde, B.; Berger, G. *Appl. Geochem.* **1998**, *13* (5), 619−629.
(13) May, H. M.; Kinniburgh, D. G.; Melmke, P. A.; Jackson, M. L. *Geochim. Cosmochim. Acta* **1986**, *50*, 1667−1677.
(14) Carroll-Webb, S. A.; Walther, J. V. *Am. J. Sci.* **1990**, *290*, 797−810.
(15) Nagy, K. L.; Blum, A. E.; Lasaga, A. C. *Am. J. Sci.* **1991**, *291*, 649−686.
(16) Wieland, E.; Stumm, W. *Geochim. Cosmochim. Acta* **1992**, *56*, 3339−3355.
(17) Ganor, J.; Mogollón, J. L.; Lasaga, A. C. *Geochim. Cosmochim. Acta* **1995**, *59*, 1037−1052.
(18) Soong, C. Ph.D. Thesis, Pennsylvania State University, PA, 1993.
(19) Devidal, J. L.; Schott, J.; Dandurand, J. L. *Geochim. Cosmochim. Acta* **1997**, *61*, 5165−5186.
(20) Chermak, J. A.; Rimstidt, J. D. *Geochim. Cosmochim. Acta* **1990**, *54*, 2979−2990.
(21) Jackson, M. L.; Lim, C. H.; Zelazny, L. W. In *Methods of Soil Analysis, Part 1: Physical and Mineralogical Methods*, 2nd ed.; Klute, A., Ed.; Soil Science Society of America: Madison, WI, 1986; pp 101−150.
(22) Man, P. P.; Klinowski, S.; Trokiner, A.; Zanni, H.; Papon, P. *Chem. Phys. Lett.* **1988**, *151*, 143−150.
(23) Murray, H. H.; Lyons, S. C. *Clays Clay Miner.* **1956**, *4*, 31−40.
(24) ICDD (International Center for Diffraction Data), Newtown Square, PA, 2000; Card No. 47-0356.
(25) ICDD (International Center for Diffraction Data), Newtown Square, PA, 2000; Card No. 50-0248.
(26) ICDD (International Center for Diffraction Data), Newtown Square, PA, 2000; Card No. 38-0513.
(27) Bickmore, B. R.; Nagy, K. L.; Young, J. S.; Drexler, J. W. *Environ. Sci. Technol.* **2001**, *35*, 4481−4486.
(28) Buhl, J.-C.; Löns, J. *J. Alloys Compd.* **1996**, *235*, 41−47.
(29) Buhl, J.-C. *Thermochim. Acta* **1991**, *178*, 19−31.
(30) Meier, W. M.; Olson, D. H. *Atlas of Zeolite Structure Types*; Structure Commission of the International Zeolite Association; Butterworth-Heinemann: London, 1992.
(31) Grundy, H. D.; Hassan, I. *Can. Mineral.* **1982**, *20*, 239−251.
(32) Hassan, I.; Grundy, H. D. *Can. Mineral.* **1991**, *29*, 377−383.
(33) Zheng, K.; Gerson, A. R.; Addai-Mensah, J.; Smart, R. St. C. *J. Cryst. Growth* **1997**, *171*, 197−208.
(34) Barnes, M. C.; Addai-Mensah, J.; Gerson, A. R. *Colloids Surf. A* **1999**, *157*, 101−116.
(35) Colella, C.; de'Gennaro, M. In *Zeolite Synthesis*; Occelli, M. L., Robson, H. E., Eds.; ACS Symposium Series 398; American Chemical Society: Washington, DC, 1989; pp 196−208.

(36) Norby, P.; Krogh Anderson, I. G.; Krogh Anderson, E.; Colella, C.; de'Gennaro, M. *Zeolites* **1991**, *11*, 248−253.
(37) Nyman, M.; Krumhansl, J. L.; Zhang, P.; Anderson, H.; Nenoff, T. M. In *Scientific Basis for Nuclear Waste Management XXIII*; Smith, R. W., Shoesmith, D. W., Eds.; Materials Research Society Symposium Proceedings Vol. 608; Materials Research Society: Boston, MA, 1999; pp 225−230.
(38) Bethke, C. M. *The Geochemist's Workbench*, Release 4.0; 2001; 224 pp.
(39) Wehrli, B.; Wieland, C.; Furrer, G. *Aquat. Sci.* **1990**, *52*, 1−29.
(40) Tits, J.; Wieland, E.; Poinssot, C.; Dobler, J. P. *Wissenschaftlicher Bericht Forschungszentrum Karlsruhe FZKA 6291*; Schüsler, W., Bauer, A., Eds.; Proceedings of the 2nd Karlsruher Geochemical Workshop; Speyer: 1999; pp 141−147.

Received for review July 18, 2002. Revised manuscript received January 22, 2003. Accepted February 12, 2003.

ES025980X